

Amplified phase shift cavity ring down spectroscopy in linear fiber cavities for sensing applications at 1550 nm

Ubaid Ullah and M. Imran Cheema *

¹Department of Electrical Engineering, Syed Babar Ali School of Science and Engineering, Lahore University of Management Sciences, Lahore 54792 Pakistan

*imran.cheema@lums.edu.pk

1 Abstract

We propose a novel optical solution that exploits the phase shift cavity ring-down technique to probe samples that induce high background noise at 1550nm. The proposed setup uses a unique design that is potentially more sensitive than the traditional fiber cavities. A tapered fiber serves as a sensing head is inserted inside the all-fiber cavity along with the amplifier. An extensive theoretical formulation is carried out to explore and optimize every aspect of the proposed setup and to enhance sensitivity while using off-the-shelf and easily accessible optical components. A generalized phase delay expression is derived while assuming tapered fiber is immersed in an analyte of known refractive index. The theoretical analysis is then followed by careful experiments. The experimental results are in good agreement with our theoretical findings. We experimentally measure glucose solution concentration employing a tapered fiber of length 0.3cm and diameter $13\mu\text{m}$. The setup offers the sensitivity of $-0.0695^\circ/\text{mM}$ and the detection limit 1mM for a $0 - 100\text{mM}$ glucose concentration range.

2 Introduction

Phase shift-cavity ring down spectroscopy (PS-CRDS) is a multipass sensitive technique independent of the source intensity fluctuations. In PS-CRDS, a CW laser source is sinusoidally modulated at an angular frequency, ω , and is injected into a cavity. The output of the cavity has a phase-shift, ϕ , compared to the input. The phase shift is directly related to the cavity ring down time, τ , as, $\tan\phi = -\omega\tau$ [1]. The change in the ring down time as a function of losses in a sample filled cavity can then be utilized for various sensing applications. For example, PS-CRDS has been utilized in numerous sensing applications for detecting gases and particles, including nitrogen dioxide [2], oxygen [3], ethene [4], acetylene [5], peroxy, organic nitrates [6], and soot particles ejecting from V2527 aircraft engine [7]. All of these applications utilize free space cavities for detection purposes.

Being a highly sensitive technique, PS-CRDS is highly attractive for chemical identification and biosensing applications. However, free space cavities are not suitable for liquid phase applications, primarily for a couple of reasons. One, the cavity becomes highly unstable due to the misalignment of optics, contamination, and the liquid inside the cavity. Second, the cavity mirrors degrade over time due to continuous contact with the liquid [8, 9]. To minimize the impact of these issues, researchers have looked over various cavity designs in terms of Brewster cavities, thin sample cells, and liquid jets inside the cavity [10]. Nevertheless, the cavity instability problem is not entirely solved, and the overall designs are also highly complicated for developing a viable liquid phase PS-CRDS sensor with free space cavities [9].

The problems mentioned above for liquid phase sensing applications can be solved by using optical fiber loops. Passive fiber loops in conjunction with the conventional cavity ring down spectroscopy (CRDS) and PS-CRDS have been used for various liquid sensing applications [11, 12, 13]. A passive loop generally contains a tapered fiber [14] or microgap [15] as a sensing head. The passive loops are typically several tens of meters and require weak couplers for coupling light into and out of the loop. Liquid phase sensing applications at 1550nm are highly attractive as various cost-effective, and off-the-shelf optical components are available to build a viable optical sensor. One of the major problems with passive loops towards biosensing or chemical identification applications is that they produce a high background absorption for aqueous solutions at 1550nm. This problem can be minimized by using an EDFA amplifier in the fiber loop [16]. CRDS in conjunction with active fiber

loops have been then utilized for various gas and liquid phase applications [17, 18, 19, 20]. An amplifier in the fiber loop minimizes the background absorption and increases the overall sensitivity and detection limit of the sensing system.

Although CRDS in an active loop improves on background liquid absorption at 1550nm, however, gain fluctuations and nonlinearity of the amplifier seriously impacts the CRDS measurements [21, 22]. It happens because in CRDS, after every round trip, the pulse strength decreases, and as a result, the amplifier response varies with varying input powers. This process distorts the exponential decay curve of the ring down time, and hence noise is added in the overall measurement.

Compared to fiber loops, a linear cavity is more sensitive for sensing measurements as the circulating optical field samples an analyte twice in one round trip, as also clearly shown in Fig. 1. This suggests that if we use PS-CRDS in linear active cavities, we can not only have a more sensitive approach at 1550nm but we can avoid the amplifier’s impact on the circulating signal. This is because in PS-CRDS, not only the signal amplitude remains constant for all times, but we also primarily measure the phase difference between the input and output sinusoid and not the signal strength. Therefore, the present work gives the first and novel scheme of an active linear cavity at 1550nm in conjunction with PS-CRDS measurements for liquid phase sensing applications.

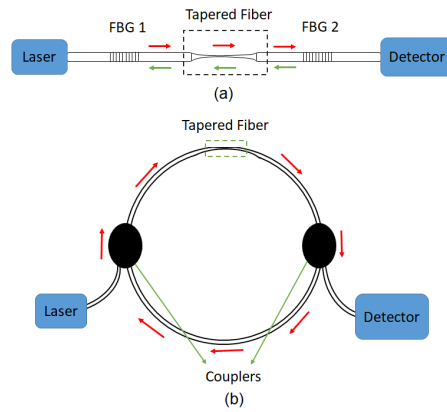


Figure 1: In one round trip, the propagating optical field in linear cavity (Fig. (a)) samples the analyte twice but the loop cavity (Fig. (b)) samples it only once.

This work theoretically determines the optimum tapered fiber diameter in an active linear cavity to maximize sensitivity for refractometric liquid sensing applications using PS-CRDS measurements. In literature, various demonstrated evanescent field sensors use either absorption [23] or refractive index change [24] of an analyte in response to a sensing event. However, a complete model will involve both the absorption and refractive index change of the analyte. Here, we consider the impact of both the absorption and refractive index changes of the liquid surrounding the tapered fiber on the output PS-CRDS signal. We experimentally measure glucose solution concentration employing a tapered fiber of length 0.3cm and diameter $13\mu\text{m}$. The setup offers the sensitivity of $-0.0695^\circ/\text{mM}$ and the detection limit 1mM for a $0 - 100\text{mM}$ glucose concentration range.

3 Theoretical Formulation

The schematics of the proposed active linear cavity with PS-CRDS measurements are shown in Fig. (2). The working principle involves applying a triangular wave for the current modulating CW tunable laser to linearly sweep the laser wavelength, ensuring that the cavity resonates periodically. An external Mach-Zehnder modulator is employed to sinusoidally modulate the laser with a frequency of ω_0 for the PS-CRDS measurements. The modulated light enters into the optical cavity through FBG 1. The light propagates through the tapered fiber (sensing head) that induces loss corresponding to the analyte under test. The forward light encounters the first circulator that guides light towards a benchtop silicon optical amplifier through port $2 \rightarrow 3$. The amplified signal completes half of the round trip after passing through port $1 \rightarrow 2$ of the second circulator and reaches FBG 2. A small portion of the light is transmitted while a large portion gets reflected. The reflected light passes through port $2 \rightarrow 3$ of circulator 2, then through port $1 \rightarrow 2$ of circulator 1, transverses tapered fiber, and finally reaches FBG 1, where it completes one round trip. Upon reflection from FBG 1, the second round trip starts. The transmitted light enters into the lock-in amplifier that provides the phase shift between cavity transmission and reference modulation signals. At the resonance, cavity build-up and relaxation time generate a maximum phase delay, which is measured as a phase dip and a transmission signal maxima on the lock-in amplifier. The out-of-resonance signal corresponds to transmission minima and phase maxima. On increasing the amplifier gain,

losses decrease in the cavity, and thus the phase shift increases. Note that as per the PS-CRDS equation, $\tan \phi = -\omega t$, the output signal lags the input signal at a resonant wavelength.

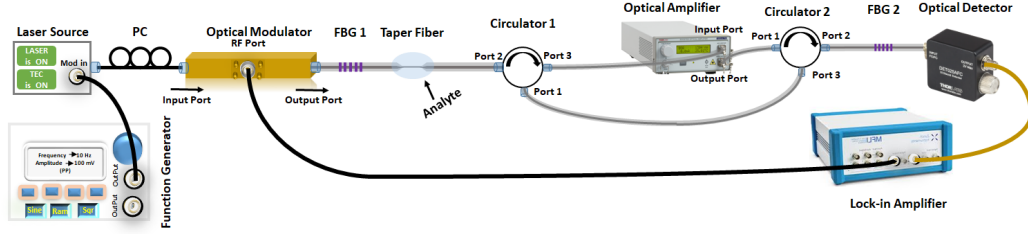


Figure 2: Schematics of the proposed experimental setup.

The signal flow diagram of the field amplitude in the cavity of the proposed setup is shown in Fig. (3), and the physical parameters of the optical components used in cavity construction are shown in Tab. (1). The overall transmission field is the superposition of several transmission terms, which denote the throughput of the cavity after successive round trips. The geometric series representing the cavity transmission is given by equations (1-2).

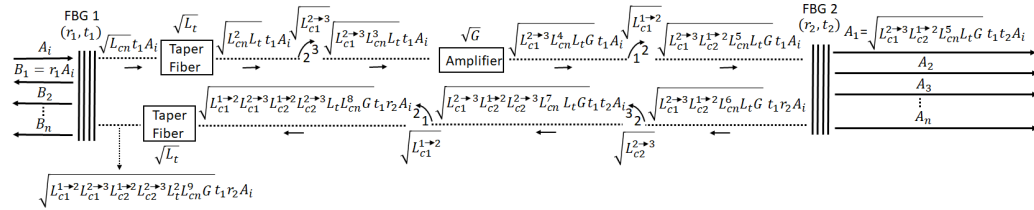


Figure 3: Signal flow diagram of the field amplified inside the optical cavity.

$$A_t = A_1 + A_2 + A_3 + \dots \quad (1)$$

$$A_t = \sqrt{L_t L_{cn}^5 L_{c1}^{2 \rightarrow 3} L_{c2}^{1 \rightarrow 2} G t_1 t_2} A_i e^{-i\delta_f} \left[1 + \sqrt{L_t^2 L_{cn}^9 L_{c1}^{1 \rightarrow 2} L_{c1}^{2 \rightarrow 3} L_{c2}^{1 \rightarrow 2} L_{c2}^{2 \rightarrow 3} G} r_1 r_2 e^{-i(\delta_f + \delta_b)} + \left(\sqrt{L_t^2 L_{cn}^9 L_{c1}^{1 \rightarrow 2} L_{c1}^{2 \rightarrow 3} L_{c2}^{1 \rightarrow 2} L_{c2}^{2 \rightarrow 3} G r_1 r_2} e^{-i(\delta_f + \delta_b)} \right)^2 + \dots \right] \quad (2)$$

| Physical Parameter | Symbol | Numerical Value [Unit] |
|--|---|----------------------------------|
| Reflectivity of FBG 1 | R_1 | 0.8568 |
| Reflectivity of FBG 2 | R_2 | 0.9992 |
| Mode index in tapered fiber | n_{tap} | $n_{tap}(n_{sol}, r_t)$ |
| Mode index in optical fiber | n_f | 1.4457 |
| Speed of light in free space | c | 2.99792458×10^8 [m/sec] |
| Modulation frequency | f_m | 3 [MHz] |
| Laser wavelength | λ_0 | 1550 [nm] |
| Insertion loss of port 1→2 (c1) | $L_{1\rightarrow 2}^{c1}$ | -0.8778 [dB] |
| Insertion loss of port 2→3 (c1) | $L_{2\rightarrow 3}^{c1}$ | -0.7857 [dB] |
| Insertion loss of port 1→2 (c2) | $L_{1\rightarrow 2}^{c2}$ | -0.57 [dB] |
| Insertion loss of port 2→3 (c2) | $L_{2\rightarrow 3}^{c2}$ | -0.60 [dB] |
| Fiber connector loss | L_{cn} | -0.15 [dB] |
| Tapered fiber constant loss | $L_t = L_{cons} + L_{ab}, L_{cons} =$ | -2 [dB] |
| Tapered fiber absorption loss | $L_t = L_{cons} + L_{ab}, L_{ab} =$ | $L_{ab}(\alpha, l_t)$ [dB] |
| Length of tapered fiber | l_t | 0.3 [cm] |
| Length of the fiber in forward direction | $l_f = l_{FBG1} + l_{taper} + l_{2\rightarrow 3}^{c1} + l_{amp} + l_{1\rightarrow 2}^{c2} + l_{FBG2}$ | 883.7 [cm] |
| Length of the fiber in reverse direction | $l_b = l_{FBG2} + l_{2\rightarrow 3}^{c2} + l_{1\rightarrow 2}^{c1} + l_{taper} + l_{FBG1}$ | 583.7 [cm] |

Table 1: Physical properties of the optical cavity involved in the proposed setup.

where δ_f denotes phase delay in the forward propagation while δ_b denotes phase delay in the reverse propagation, which makes a complete round trip inside an optical cavity. The following expressions define δ_f and δ_b , respectively.

$$\begin{aligned}\delta_f &= \frac{2\pi n_f l_f}{\lambda_0} + \frac{2\pi n_t l_t}{\lambda_0} \\ \delta_b &= \frac{2\pi n_f l_b}{\lambda_0} + \frac{2\pi n_t l_t}{\lambda_0}\end{aligned}\quad (3)$$

We use the geometric series's following property to simplify and rewrite the transmission field equation in a closed-form expression.

$$1 + \chi + \chi^2 + \chi^3 + \dots = 1/(1 - \chi) \quad \text{for } 0 < \chi < 1 \quad (4)$$

The transmission field equation is then simplified to the following form:

$$A_t = \frac{\sqrt{L_t L_{cn}^5 L_{c1}^{2 \rightarrow 3} L_{c2}^{1 \rightarrow 2}} G t_1 t_2 A_i e^{-i\delta_f}}{1 - \sqrt{L_t^2 L_{cn}^9 L_{c1}^{1 \rightarrow 2} L_{c1}^{2 \rightarrow 3} L_{c2}^{1 \rightarrow 2} L_{c2}^{2 \rightarrow 3}} G r_1 r_2 e^{-i(\delta_f + \delta_b)}} \quad (5)$$

where,

$$\chi = \sqrt{L_t^2 L_{cn}^9 L_{c1}^{1 \rightarrow 2} L_{c1}^{2 \rightarrow 3} L_{c2}^{1 \rightarrow 2} L_{c2}^{2 \rightarrow 3}} G r_1 r_2 \quad (6)$$

Now the transmittance T is defined as the ratio of transmitted intensity ($A_t A_t^*$) to the input intensity ($A_i A_i^*$) and is given by:

$$\begin{aligned}T &= \frac{L_{cn}^5 L_t L_{c1}^{2 \rightarrow 3} L_{c2}^{1 \rightarrow 2} G (t_1 t_2)^2}{\left(1 - \sqrt{L_t^2 L_{cn}^9 L_{c1}^{1 \rightarrow 2} L_{c1}^{2 \rightarrow 3} L_{c2}^{1 \rightarrow 2} L_{c2}^{2 \rightarrow 3}} G r_1 r_2\right)^2} \\ &\quad + 4 \sqrt{L_t^2 L_{cn}^9 L_{c1}^{1 \rightarrow 2} L_{c1}^{2 \rightarrow 3} L_{c2}^{1 \rightarrow 2} L_{c2}^{2 \rightarrow 3}} G r_1 r_2 \sin^2((\delta_f + \delta_b)/2)\end{aligned}\quad (7)$$

The transmission and reflection coefficients are defined as follows:

$$r_1 = \sqrt{R_1}, \quad r_2 = \sqrt{R_2}, \quad t_1 = \sqrt{1 - R_1}, \quad t_2 = \sqrt{1 - R_2} \quad (8)$$

We obtain the following final transmission expression by substituting the above mentioned parameters:

$$\begin{aligned}T &= \frac{L_{cn}^5 L_t L_{c1}^{2 \rightarrow 3} L_{c2}^{1 \rightarrow 2} G (1 - R_1)(1 - R_2)}{\left(1 - \sqrt{L_t^2 L_{cn}^9 L_{c1}^{1 \rightarrow 2} L_{c1}^{2 \rightarrow 3} L_{c2}^{1 \rightarrow 2} L_{c2}^{2 \rightarrow 3}} G r_1 r_2\right)^2} \\ &\quad \left[+ 4 \sqrt{L_t^2 L_{cn}^9 L_{c1}^{1 \rightarrow 2} L_{c1}^{2 \rightarrow 3} L_{c2}^{1 \rightarrow 2} L_{c2}^{2 \rightarrow 3}} G \sqrt{R_1 R_2} \sin^2((\delta_f + \delta_b)/2) \right]\end{aligned}\quad (9)$$

We can see that if we assume that gain and losses are equal and $R_1 = R_2 = R$ then Eq. (9) reduces to the following standard Fabry-Perot equation:

$$T = \frac{(1 - R)^2}{(1 - R)^2 + 4R \sin^2((\delta_f + \delta_b)/2)} \quad (10)$$

This suggests the correctness of our derived expression. We are also interested in the full width half maximum (FWHM) of our proposed active cavity as FWHM will help us determine the phase expression for PS-CRDS calculations. The maximum possible transmission of the proposed setup is given by the following equation:

$$T_0 = \frac{L_{cn}^5 L_t L_{c1}^{2 \rightarrow 3} L_{c2}^{1 \rightarrow 2} G (1 - R_1) (1 - R_2)}{\left(1 - \sqrt{L_t^2 L_{cn}^9 L_{c1}^{1 \rightarrow 2} L_{c1}^{2 \rightarrow 3} L_{c2}^{1 \rightarrow 2} L_{c2}^{2 \rightarrow 3} G R_1 R_2}\right)^2} \quad (11)$$

From equation (9) and equation (11), the following condition needs to be satisfied for determining the half width half maximum, HWHM (represented by subscript 1/4), :

$$\frac{L_{cn}^5 L_t L_{c1}^{2 \rightarrow 3} L_{c2}^{1 \rightarrow 2} G (1 - R_1) (1 - R_2)}{2 * \left(1 - \sqrt{L_{cn}^9 L_t^2 L_{c1}^{1 \rightarrow 2} L_{c1}^{2 \rightarrow 3} L_{c2}^{1 \rightarrow 2} L_{c2}^{2 \rightarrow 3} G R_1 R_2}\right)^2} = \frac{L_{cn}^5 L_t L_{c1}^{2 \rightarrow 3} L_{c2}^{1 \rightarrow 2} G (1 - R_1) (1 - R_2)}{\left(1 - \sqrt{L_{cn}^9 L_t^2 L_{c1}^{1 \rightarrow 2} L_{c1}^{2 \rightarrow 3} L_{c2}^{1 \rightarrow 2} L_{c2}^{2 \rightarrow 3} G r_1 r_2}\right)^2 + 4 \sqrt{L_{cn}^9 L_t^2 L_{c1}^{1 \rightarrow 2} L_{c1}^{2 \rightarrow 3} L_{c2}^{1 \rightarrow 2} L_{c2}^{2 \rightarrow 3} G} \sqrt{R_1 R_2} \sin^2\left(\frac{(\delta_f + \delta_b)_{1/4}}{2}\right)} \quad (12)$$

It can easily be shown that equation (12) reduces to the following form:

$$\sin\left(\frac{(\delta_f + \delta_b)_{1/4}}{2}\right) = \frac{1}{2} \left[\frac{1}{\sqrt{\chi}} - \sqrt{\chi} \right] \quad (13)$$

where χ is given by equation (6). In the proposed active Fabry-Perot cavity, the transmission peaks will be much narrower than the FSR of the cavity, therefore, assuming $\frac{(\delta_f + \delta_b)_{1/4}}{2} \ll \frac{\pi}{2}$, then equation (13) can be written as:

$$\left(\frac{(\delta_f + \delta_b)_{1/4}}{2}\right) = \frac{1}{2} \left[\frac{1}{\sqrt{\chi}} - \sqrt{\chi} \right] \quad (14)$$

Compared to HWHM, FWHM (represented by subscript 1/2) is two times in width, therefore,

$$(\delta_f + \delta_b)_{1/2} = \Delta\delta_{1/2} = 2 \left[\frac{1}{\sqrt{\chi}} - \sqrt{\chi} \right] \quad (15)$$

In the wavelength domain, the following expression represents FWHM:

$$\Delta\lambda_{1/2} = \frac{\lambda_0^2 \left(\frac{1}{\sqrt{\chi}} - \sqrt{\chi} \right)}{\pi [n_f(l_f + l_b) + 2n_{tap}l_t]} \quad (16)$$

For a standard passive Fabry-Perot cavity (see Fig. 1a) based on two FBGs with $R_1 = R_2 = R$ and without any tapered fiber including $l_f = l_b = l$, then equation 16 reduces to the standard FWHM expression:

$$\Delta\lambda_{1/2} = \frac{\lambda_0^2(1 - R)}{2\pi n_f l \sqrt{R}} \quad (17)$$

The loss of the cavity is directly proportional to FWHM. If the gain is equal to all losses in the cavity and $R_1 = R_2 = 1$ then it represents a lossless cavity. FWHM will be zero in this ideal cavity, as can also be seen from equation (16).

$$\Delta\lambda_{1/2} = \frac{\lambda_0^2(1 - 1)}{\pi [n_f(l_f + l_b) + 2n_{tap}l_t]} = 0, \quad \text{As } \sqrt{\chi} = 1 \quad (18)$$

On the other extreme, if we assume that maximum possible loss inside the cavity, i.e., $R_1 = R_2 = 0$, then FWHM will become infinite as can be seen in the following:

$$\Delta\lambda_{1/2} = \infty \quad \text{When } \lim_{\sqrt{\chi} \rightarrow 0} \frac{1}{\sqrt{\chi}} \rightarrow \infty \quad (19)$$

The results in equations (17-19) suggest the correctness of the FWHM expression in equation (16).

3.1 PS-CRDS sensing principle of the proposed cavity

The proposed setup employs an amplitude modulated laser source to excite the cavity. The light inside the cavity passes through the tapered fiber, optical circulators, and amplifier multiple times before it decays down to

zero. The decay time is related to the phase delay between the cavity output and the reference modulating signal according to the following PS-CRDS relationship [1]:

$$\tan \phi = -\omega_m \tau \quad (20)$$

where ω_m is the modulation frequency. The amplifier gain is used for overcoming background absorption that is usually induced by liquids at 1550nm. The ring down time will increase with an increase in the gain, and hence the phase, ϕ , will also increase.

A change in the analyte concentration represents a change in the tapered fiber's surrounding refractive index (RI). Therefore, when the concentration increases, the optical mode is pushed out of the tapered fiber and experiences a loss. Simultaneously, the analyte concentration will also induce absorption loss to the evanescent field of the propagating mode. These losses decrease the cavity's ring down time, and hence the phase, ϕ , also reduces. The ring down time of a cavity is also related to its FWHM, as can be easily shown from energy conservation principles [25],

$$\frac{\lambda_0}{\Delta\lambda_{1/2}} = \omega_0 \tau \quad (21)$$

where ω_0 is the optical frequency. Substituting τ from equation (21) in equation 20, we obtain

$$\phi = \tan^{-1} \left(\frac{f_m \lambda_0^2}{(c/n_f) \Delta\lambda_{1/2}} \right) \quad (22)$$

where $\Delta\lambda_{1/2}$ is given by equation (16).

4 Simulation results

We assume that a tapered fiber is immersed in aqueous glucose solutions of various concentrations for generating simulation results. We use the following expression for determining refractive indices of glucose solutions [26]:

$$n_{sol} = x_0(\lambda) + y_0(\lambda)C_g \quad (23)$$

where $x_0 = 1.318$ is the refractive index of DI water at room temperature and 1550nm [27], $y_0 = 6.5998 \times 10^{-4}$ denotes a conversion slope between

glucose concentration and solution refractive indices, and C_g stands for glucose concentration measured in mM. These values and equation (23) indicate that the glucose solution's refractive index increases with an increase in glucose. Therefore, when we immerse a tapered fiber in the solution, the tapered fiber's leaked evanescent field increases as the glucose concentration increases—consequently, the ring down time and hence phase, ϕ changes.

The tapered fiber diameter also influences the evanescent field strength; the thinner the tapered fiber, the stronger the evanescent field and vice versa. This suggests that for achieving maximum sensitivity, there will be an interplay between the tapered fiber diameter and the analyte concentration as both impact the evanescent field strength. Hence, an optimum tapered fiber diameter may be present for achieving high sensitivity for detecting glucose concentrations. To explore the optimized tapered fiber diameter, let us look at the fraction of the evanescent field outside the tapered fiber, i.e., the ratio of evanescent field power to the total optical power in a cross-sectional area of the tapered fiber, and is given below:

$$\Gamma = \frac{\int_{r_t}^{\infty} P(r, \phi) r dr d\phi}{\int_0^{\infty} P(r, \phi) r dr d\phi} \quad (24)$$

We use the finite element method to determine Γ of a range of tapered fiber diameters for various lossless glucose concentration solutions. For each tapered fiber radius, we obtain a linear curve of Γ as a function of glucose concentrations. We then plot each curve slope against the tapered fiber's corresponding radius, as shown in Fig. (4). Each data point is generated for refractive index changes of $10^{-4} - 10^{-2}$. It is clear from the plot that as we decrease the tapered fiber's radius from a relatively larger value, there is a gradual increase in the sensitivity. The sensitivity increases drastically when the tapered fiber's diameter is near the source wavelength. The increase in the sensitivity trend keeps going up to a critical tapered fiber radius, after which this trend flips, and the sensitivity starts decreasing with a decrease in the tapered fiber radius. The critical tapered fiber radius is also specific to the analyte.

Physically, as the tapered fiber's radius decreases from $10\mu m$ the evanescent field and the power density inside the tapered fiber increase. The increase in the power density ensures relatively large changes in Γ for small refractive index changes. Near the critical radius, the power density increases dramatically as the fiber's radius becomes comparable to the source

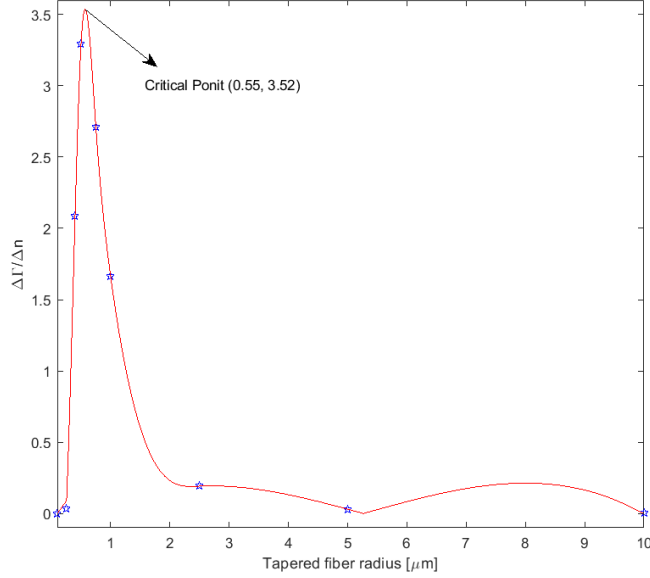


Figure 4: The evanescent field changes for given RI changes as a function of tapered fibers radii. Each data point is generated for a refractive index change of $(10^{-4} - 10^{-2})$.

wavelength. At this point, changes in Γ due to refractive index changes are also maximum. The critical radius is $0.55\mu m$ for glucose solution, as shown in Fig. (4). The propagating mode becomes loosely intact with the tapered fiber after the critical radius, and hence the change in Γ due to the change in the refractive index of the solution decreases.

After looking at the impact on sensitivity due to analyte concentrations and tapered fiber diameter, let us look at the influence of glucose absorption losses on the sensitivity. The tapered fiber loss can be due to static and/or dynamic losses. Static losses are constant and occur due to structural deformations and impurities accumulation during the taper drawing process. On the other hand, the dynamic losses vary with the analyte concentrations. These include absorption due to the analyte as well as background water. The following expression gives the total absorption coefficient, α , of a glucose aqueous solution relative to air [28]:

$$\alpha = \Gamma\alpha_w C_w + \Gamma\alpha_g C_g - \Gamma\alpha_w f_w^g C_g \quad (25)$$

where α_w is the absorption coefficient of DI water, α_g absorption coefficient

of glucose, C_w is the DI water concentration, C_g is the glucose concentration, and f_w^g is the water displacement coefficient of glucose. In equation (25), the first and second terms represent absorption due to water and glucose. The last term deducts a portion of water absorption from that solution part, which is replaced by glucose. It is mandatory to include refractive index changes to understand the whole picture of a solution's absorption process. The increase in the concentration of a solution brings two effects in the picture, i.e., a change in the refractive index and a change in the solution's absorption. Furthermore, the refractive index's increase enhances the evanescent field and a corresponding increase in Γ of the tapered fiber. The large evanescent field interacts with a large solution portion, and hence, the absorption loss increases, as shown in equation (25). In parallel, an increase in glucose concentration also changes the absorption loss of the solution such that, if $\alpha_g < \alpha_w f_w^g$, there is a decrease in the absorption loss while for $\alpha_g > \alpha_w f_w^g$ the absorption loss increases. The solution's net absorption loss is a combined effect of an increase in the loss due to the evanescent field and a change in the absorption loss due to increased glucose concentration.

We obtain a linear curve of Γ as a function of glucose concentrations. We then plot each curve slope against the tapered fiber's corresponding radius, as shown in Fig. (4). Each data point is generated for refractive index changes of $10^{-4} - 10^{-2}$.

For the current work, we use $\alpha_w = 1.45 \times 10^{-4}(mM)^{-1}cm^{-1}$ [27], $C_w = 55135mM$, $C_g = (0 - 15.15)mM$, $\alpha_g = 7.23 \times 10^{-4}(mM)^{-1}cm^{-1}$ [28], and $f_w^g = 6.245$ [28]. We again employ finite element method simulations along with equations (24-25) and obtain linear curves of α as a function of glucose concentrations. We then plot each curve slope against the tapered fiber's corresponding radius, as shown in Fig. (5). The blue plot considers only water absorption loss, i.e., an ideal solution that has the same absorption coefficient as water but induces refractive index changes equivalent to glucose solutions. In contrast, the orange plot considers both water and glucose absorption losses for glucose solutions. In the case of glucose solution $\alpha_g < \alpha_w f_w^g$, which indicates that the addition of glucose will reduce the solution's absorption loss compared to pure DI water [29]. Numerically, it is also evident from Fig. (5) inset. In the plot, it is clear that the absorption loss is always lower when we also include glucose absorption loss as compared to water with only refractive index changes. We assume a glucose concentration of $(0 - 15.15mM)$ in our analysis. As discussed earlier, the absorption loss coefficient has two sources. In the case of glucose solution, the prominent contribution

is due to the increase in the refractive index with glucose concentration.

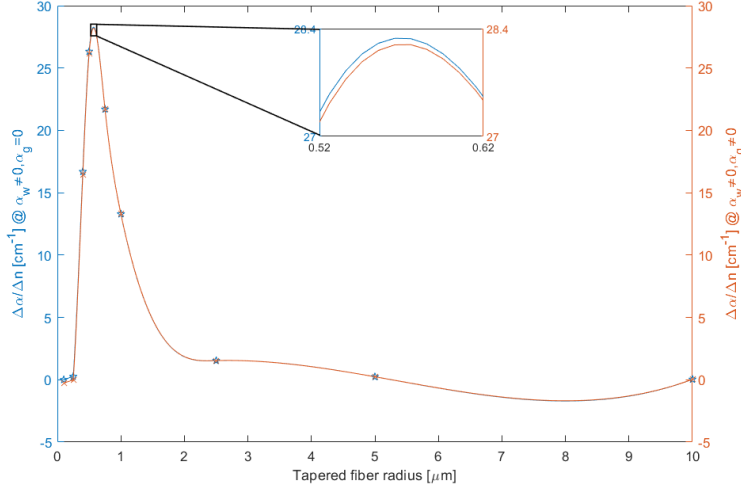


Figure 5: The overall tapered fiber absorption changes (see equation (25)) for given RI changes as a function of tapered fibers radii. Each data point is generated for a glucose solution of concentrations (0 – 15.15)*mM*.

The following expression now represents the overall loss experienced by the tapered fiber:

$$L_{ab} = e^{-\alpha l_t} \quad (26)$$

where l_t is the tapered fiber length. The overall tapered fiber loss is represented by $L_t = L_{cons} + L_{ab}$. Now using parameters listed in Tab. (1), previously mentioned finite element method simulations, and equations (19,22-26), we determine phase, ϕ , for various glucose concentrations at different amplifier gains. A representative result of ϕ as a function of glucose concentrations at an amplifier gain is shown in Fig. (6). We also plot the phase shift for various glucose concentrations against the amplifier gain, as shown in Fig. (7). We assume the optimum tapered fiber of radius, $r_t = 0.5\mu m$ in these simulation results.

5 Experimental Results

For the proposed active cavity setup, this section provides various experimental results including determining the amount of glucose in aqueous solutions.

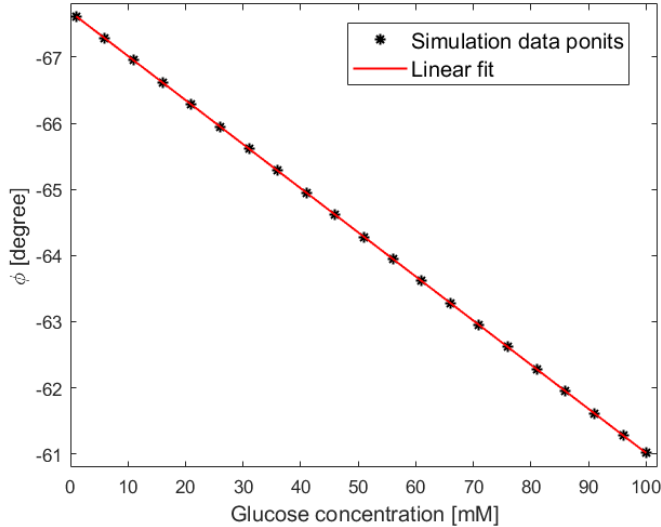


Figure 6: Simulated phase shift as a function of glucose concentration for $1.1\mu\text{m}$ diameter tapered fiber at 6dB amplifier gain

5.1 Phase and amplitude peaks as a function of the wavelength scan

A representative amplified PS-CRDS measurement for the active cavity setup (see Fig. (2)) is shown in Fig. (8). We notice that resonance peaks are not synchronized with phase dips in wavelength positions; instead, phase minimum is red and blue-shifted during the decreasing and increasing wavelength scans, respectively. We will use the coupled mode (CM) theory to explain this behavior. The fundamental CM equation for a linear optical cavity is given below [30]:

$$\frac{dE_{cav}}{dt} = j\omega_{0m}E_{cav} - \left(\frac{1}{\tau}\right)E_{cav} + \kappa E_{ip} \quad (27)$$

where E_{cav} denotes the cavity field, ω_0 represents the cavity resonance frequency, τ is the cavity ring down time, κ is the field coupling coefficient at FBG1, and E_{ip} is the cavity input field. The ring down time, τ , can be represented as:

$$\frac{1}{\tau} = \frac{1}{\tau_0} + \frac{1}{\tau_{e1}} + \frac{1}{\tau_{e2}} \quad (28)$$

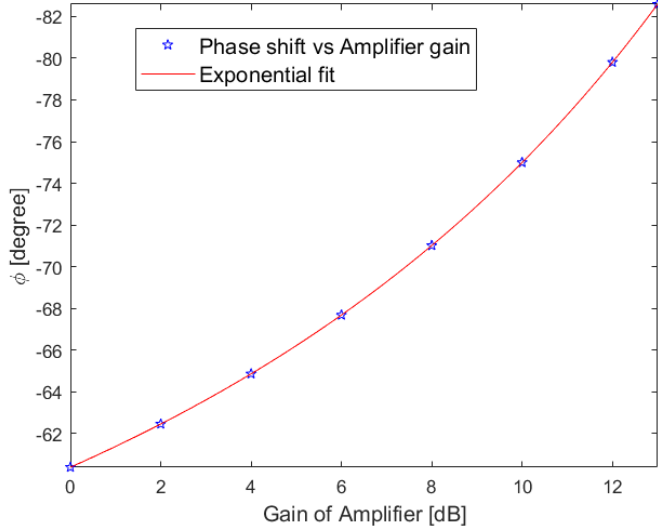


Figure 7: Simulated phase shift as a function of the amplifier gain. Each data point is generated for a glucose solution of concentration ($0 - 15.15mM$).

where τ_o represents photon life time due to internal losses of the cavity, e.g., in our case it will represent losses due to intrinsic SMF-28 fiber attenuation and losses due to the tapered fiber and associated sensing mechanisms. The coupling life times or photon lifetimes, τ_{e1}, τ_{e2} , are due to transmission losses at FBG1 and FBG2, respectively and are given by the following relations:

$$\tau_{e1} = \frac{n_f l}{c(1 - R_1)} \quad (29)$$

$$\tau_{e2} = \frac{n_f l}{c(1 - R_2)} \quad (30)$$

where l is the cavity length. The coupling coefficient, κ , is then given by the following equation [30]:

$$\sqrt{\frac{2}{\tau_{e1}}} \quad (31)$$

In PS-CRDS setup, an optical cavity is excited by a modulated laser light with modulation frequency ω_m and optical frequency ω . Note that ω is the scan frequency of the current tuned laser. The input field, E_{ip} can then be

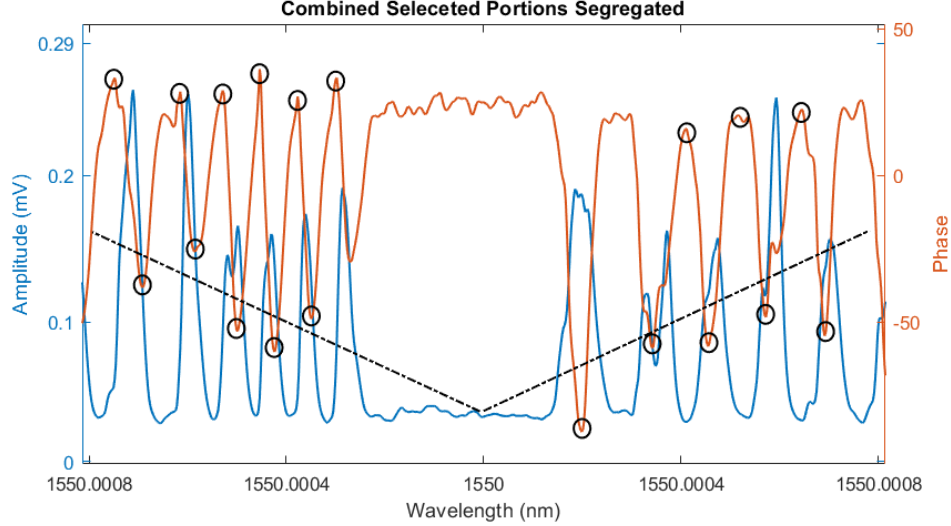


Figure 8: Representative amplified PS-CRDS experimental data. The black dotted line is the wavelength scan signal. The blue and red curves are amplitude and phase data, respectively. The circles on the phase curve are data points for determining the phase for a glucose concentration.

modeled as the positive optical frequency and positive modulation frequency component of $E_{in}\cos(\omega_m t)\cos(\omega)$ as given below:

$$E_{ip} = \frac{e^{j(\omega+\omega_m)t}}{4} E_{in} \quad (32)$$

We can now solve differential equation (27) with the sinusoidal input, E_{ip} , and obtain the following result:

$$E_{cav} = \sqrt{\frac{2}{\tau_{e1}}} \frac{e^{j(\omega+\omega_m)t} - e^{(j\omega_0 - \frac{1}{\tau}t)}}{(1 + j\tau(\omega + \omega_m - \omega_0))} E_{in} \quad (33)$$

At the steady state, the cavity field reduces to the following form:

$$E_{cav} = \frac{\sqrt{\frac{2}{\tau_{e1}}} \tau e^{j(\omega+\omega_m)t}}{4(1 + j\tau(\omega + \omega_m - \omega_0))} E_{in} \quad (34)$$

We can find the cavity output field by multiplying the cavity field, equation (34) with the FBG2 coupling coefficient and is given below:

$$E_{op} = \kappa_{e2} E_{cav} = \sqrt{\frac{2}{\tau_{e2}}} E_{cav} = \frac{\tau e^{j(\omega+\omega_m)t}}{2\sqrt{\tau_{e1}\tau_{e2}}(1 + j\tau(\omega + \omega_m - \omega_0))} E_{in} \quad (35)$$

Using equations (29-30), the magnitude of the output field is given by the following equation.

$$|E_{op}| = \frac{c\tau\sqrt{(1-R_1)(1-R_2)}}{2n_f l\sqrt{(1+\tau^2(\omega+\omega_m-\omega_0)^2)}}|E_{in}| \quad (36)$$

We now obtain the PS-CRDS phase delay, ϕ , by taking the ratio of imaginary to real parts of equation (35), i.e.,

$$\tan\phi = -(\omega+\omega_m-\omega_0)\tau \quad (37)$$

At a resonant frequency, $\omega = \omega_0$, equations (36)-(36) reduce to the standard PS-CRDS equations [3]. A physical interpretation of equations (36-37) explains the red and blue shifts of phase dips relative to resonance peaks. As shown in equation (36), maximum amplitude $|E_{op}|$ occurs at $\omega+\omega_m = \omega_0$ for a resonance peak. While it is evident from equation (37) that a phase dip maxima requires $\omega+\omega_m > \omega_0$ condition. In the upward frequency scan, the condition $\omega+\omega_m > \omega_0$ is true after the resonance peak point, i.e., $\omega+\omega_m > \omega_0$ near the vicinity of the resonance peak and hence the blue shift in wavelength. Similarly, in the frequency downward scan, $\omega+\omega_m > \omega_0$ becomes true before the resonance peak point, i.e., $\omega+\omega_m > \omega_0$ and hence the red shift in wavelength. It should be noted that the trend of wavelength shifts of phase dips with respect to amplitude peaks is true for both passive and active cavities in which PS-CRDS measurements are conducted by wavelength tuning the laser source.

5.2 Phase as a function of the amplifier gain

Here, we look at the amplifier gain impact on the PS-CRDS phase measurements. The increase in the amplifier gain increases the cavity phase delay as the light will stay longer inside the cavity. Fig. (9) shows the increase in the phase delay with respect to amplifier gain for a tapered fiber of diameter $13\mu m$ placed in the open air. The amplifier gain can compensate for losses inside the cavity and bring the sensing event into the detection limit that may be masked by the strong background absorption at 1550nm.

5.3 Detection of glucose in aqueous solutions

This section presents our experimental results of sensing glucose in aqueous solutions using our amplified PS-CRDS setup. First, we prepare various

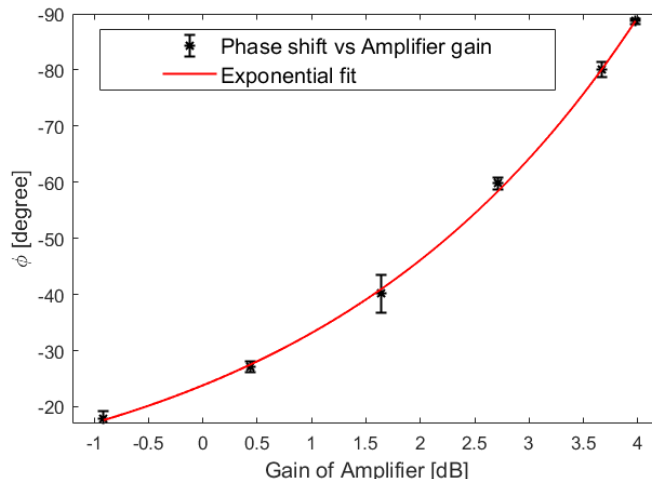


Figure 9: Experimentally observed phase shift as a function of the amplifier gain. We use a tapered fiber of diameter $\approx 13\mu m$ and is placed in air. All other experimental parameters are tabulated in Tab. (1).

concentrations of glucose solutions. These solutions are then injected into a custom-made fluidic cell containing the tapered fiber via a standard syringe. We wash the tapered fiber and the fluidic cell thoroughly with DI water before measurements. The laser is current tuned by a triangular signal of amplitude $100mV_{pp}$ and frequency $10Hz$. The current tuning enables the laser wavelength to be swept over a range of $45pm$ and centered at $1550nm$ to obtain the PS-CRDS data, as shown in the representative Fig. (8). We obtain absolute phase shifts by subtracting the phase minimum and maximum for a resonance peak as shown with black circles in Fig. (8). The absolute phases are then averaged to produce a single-phase measurement for an injected sample. To produce the error bars, we repeat measurements three times for each glucose concentration. The measured phase delay for various glucose concentrations is shown in Fig. (10). From the experimental data, we obtain the sensitivity and detection limit of $-0.0695degree/mM$ and $1mM$, respectively.

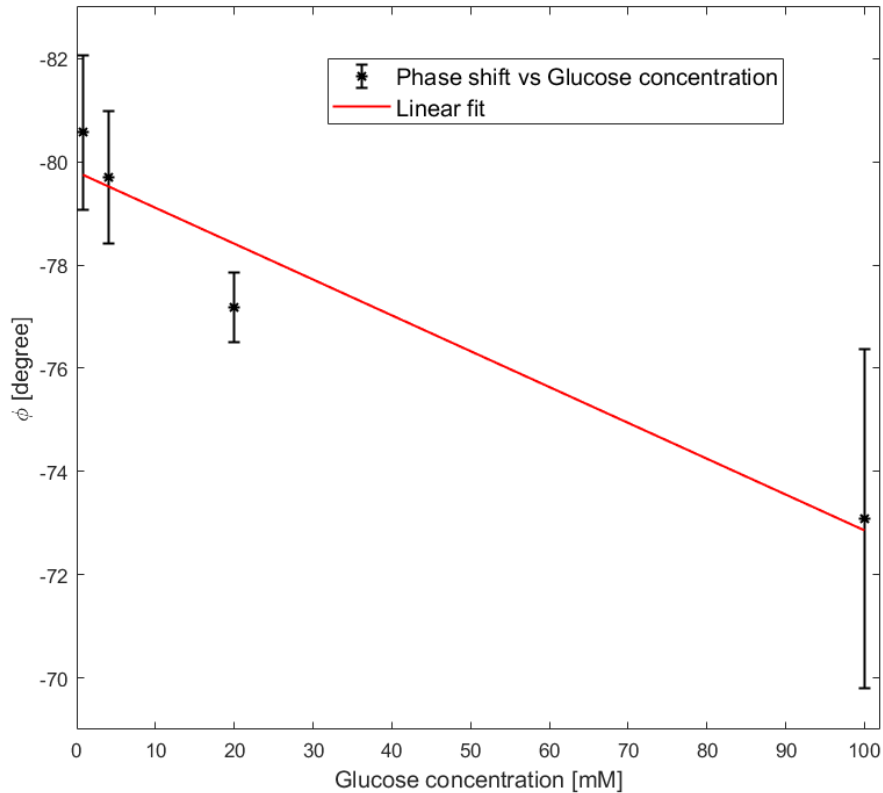


Figure 10: Experimental results for PS-CRDS phase shift as a function of glucose concentrations.

6 Conclusions

We develop novel ideas to enhance the sensitivity of the amplified PS-CRDS setup employing tapered fiber as a sensing head. The proposed setup allows light to transverse through the tapered fiber twice in one round trip and doubles the sensitivity compared to the conventional fiber loops. To further enhance the sensitivity, we present a theoretical model that accounts for both absorption and refractive index changes with the analyte concentration changes. The model can predict an optimum diameter of the tapered fiber, maximizing the sensitivity for a specific analyte. We anticipate that this work will find many applications in biosensing and chemical analysis.

References

- [1] Giel Berden and Richard Engeln. *Cavity ring-down spectroscopy: techniques and applications*. John Wiley & Sons, 2009.
- [2] Paul L Kebabian, Ezra C Wood, Scott C Herndon, and Andrew Freedman. A practical alternative to chemiluminescence-based detection of nitrogen dioxide: Cavity attenuated phase shift spectroscopy. *Environmental science & technology*, 42(16):6040–6045, 2008.
- [3] Richard Engeln, Gert von Helden, Giel Berden, and Gerard Meijer. Phase shift cavity ring down absorption spectroscopy. *Chemical Physics Letters*, 262(1-2):105–109, 1996.
- [4] Roberto Grilli, Luca Ciaffoni, and Andrew J Orr-Ewing. Phase-shift cavity ring-down spectroscopy using mid-ir light from a difference frequency generation ppln waveguide. *Optics letters*, 35(9):1383–1385, 2010.
- [5] Chris Hovde and Anthony L Gomez. Phase-shift feedback cavity ring-down spectroscopy. *Applied optics*, 54(17):5555–5559, 2015.
- [6] Yasuhiro Sadanaga, Ryo Takaji, Ayana Ishiyama, Kazuo Nakajima, Atsushi Matsuki, and Hiroshi Bandow. Thermal dissociation cavity attenuated phase shift spectroscopy for continuous measurement of total peroxy and organic nitrates in the clean atmosphere. *Review of Scientific Instruments*, 87(7):074102, 2016.
- [7] Zhenhong Yu, Luke D Ziemba, Timothy B Onasch, Scott C Herndon, Simon E Albo, Richard Miake-Lye, Bruce E Anderson, Paul L Kebabian, and Andrew Freedman. Direct measurement of aircraft engine soot emissions using a cavity-attenuated phase shift (caps)-based extinction monitor. *Aerosol Science and Technology*, 45(11):1319–1325, 2011.
- [8] Claire Vallance and Cathy M Rushworth. Cavity ringdown spectroscopy for the analysis of small liquid volumes. In *Cavity-Enhanced Spectroscopy and Sensing*, pages 385–410. Springer, 2014.
- [9] Jonathan E Thompson. Cavity-enhanced spectroscopy in condensed phases: Recent literature and remaining challenges. *Journal of Spectroscopy*, 2017, 2017.

- [10] Cathy M Rushworth, Joanna Davies, João T Cabral, Philip R Dolan, Jason M Smith, and Claire Vallance. Cavity-enhanced optical methods for online microfluidic analysis. *Chemical Physics Letters*, 554:1–14, 2012.
- [11] Helen Waechter, Klaus Bescherer, Christoph J Durr, Richard D Oleschuk, and Hans-Peter Loock. 405 nm absorption detection in nanoliter volumes. *Analytical chemistry*, 81(21):9048–9054, 2009.
- [12] Runkai Li, Hans-Peter Loock, and Richard D Oleschuk. Capillary electrophoresis absorption detection using fiber-loop ring-down spectroscopy. *Analytical chemistry*, 78(16):5685–5692, 2006.
- [13] Jack Barnes, Marian Dreher, Krista Plett, R Stephen Brown, Cathleen M Crudden, and Hans-Peter Loock. Chemical sensor based on a long-period fibre grating modified by a functionalized polydimethylsiloxane coating. *Analyst*, 133(11):1541–1549, 2008.
- [14] Rana M Armaghan Ayaz, Yigit Uysalli, Berna Morova, Nima Bavili, Ubaid Ullah, M Daniyal Ghauri, M Imran Cheema, and Alper Kiraz. Linear cavity tapered fiber sensor using mode-tracking phase-shift cavity ring-down spectroscopy. *JOSA B*, 37(6):1707–1713, 2020.
- [15] Zhaoguo Tong, Alexander Wright, Theresa McCormick, Runkai Li, Richard D Oleschuk, and Hans-Peter Loock. Phase-shift fiber-loop ring-down spectroscopy. *Analytical chemistry*, 76(22):6594–6599, 2004.
- [16] George Stewart, Kathryn Atherton, Hongbo Yu, and Brian Culshaw. An investigation of an optical fibre amplifier loop for intra-cavity and ring-down cavity loss measurements. *Measurement Science and Technology*, 12(7):843, 2001.
- [17] George Stewart, Kathryn Atherton, and Brian Culshaw. Cavity-enhanced spectroscopy in fiber cavities. *Optics letters*, 29(5):442–444, 2004.
- [18] K Liu, TG Liu, GD Peng, JF Jiang, HX Zhang, DG Jia, Y Wang, WC Jing, and YM Zhang. Theoretical investigation of an optical fiber amplifier loop for intra-cavity and ring-down cavity gas sensing. *Sensors and Actuators B: Chemical*, 146(1):116–121, 2010.

- [19] Kavita Sharma, Sijing Liang, Shaif-ul Alam, Shanti Bhattacharya, Deepa Venkitesh, and Gilberto Brambilla. Fiber-based cavity ring-down technique for refractive index sensing at 1953 nm using tapered fibers. *IEEE sensors letters*, 1(3):1–4, 2017.
- [20] Kavita Sharma, MIM Abdul Khudus, SU Alam, Shanti Bhattacharya, Deepa Venkitesh, and Gilberto Brambilla. Comparison of detection limit in fiber-based conventional, amplified, and gain-clamped cavity ring-down techniques. *Optics Communications*, 407:186–192, 2018.
- [21] Tongwei Chu, Pengpeng Wang, and Cunguang Zhu. Modeling of active fiber loop ring-down spectroscopy considering gain saturation behavior of edfa. *Journal of Lightwave Technology*, 38(4):966–973, 2019.
- [22] Tongwei Chu, Cunguang Zhu, and Pengpeng Wang. Modeling of active fiber loop ring-down spectroscopy considering non-linear effects of edfa gain. *IEEE Sensors Journal*, 2020.
- [23] Peter B Tarsa, Paul Rabinowitz, and Kevin K Lehmann. Evanescent field absorption in a passive optical fiber resonator using continuous-wave cavity ring-down spectroscopy. *Chemical Physics Letters*, 383(3-4):297–303, 2004.
- [24] N Ni, CC Chan, L Xia, and P Shum. Fiber cavity ring-down refractive index sensor. *IEEE Photonics Technology Letters*, 20(16):1351–1353, 2008.
- [25] John David Jackson. *Classical electrodynamics*. John Wiley & Sons, 2007.
- [26] Yen-Liang Yeh. Real-time measurement of glucose concentration and average refractive index using a laser interferometer. *Optics and Lasers in Engineering*, 46(9):666–670, 2008.
- [27] George M Hale and Marvin R Query. Optical constants of water in the 200-nm to 200- μ m wavelength region. *Applied optics*, 12(3):555–563, 1973.
- [28] Airat K Amerov, Jun Chen, and Mark A Arnold. Molar absorptivities of glucose and other biological molecules in aqueous solutions over the

first overtone and combination regions of the near-infrared spectrum. *Applied Spectroscopy*, 58(10):1195–1204, 2004.

- [29] Zhong Hai He and Guang Shuai Zhu. Variation of absorption coefficient of glucose water in consideration of water displacement. In *Advanced Materials Research*, volume 159, pages 358–362. Trans Tech Publ, 2011.
- [30] Hermann A Haus. *Waves and fields in optoelectronics*. Prentice-Hall, 1984.